

ARTICLE OPEN



Effect of nitrogen content on corrosion behavior of high-nitrogen austenitic stainless steel

Fengyin Gao¹, Yanxin Qiao¹✉, Jian Chen²✉, Lanlan Yang¹, Huiling Zhou¹, Zhibin Zheng³✉ and Lianmin Zhang⁴

A series of electrochemical tests combined with the techniques of scanning electron microscopy (SEM), electron backscatter diffraction (EBSD) and X-ray photoelectron spectroscopy (XPS) were used to study the effect of nitrogen content on the composition, structure and protectiveness of passive films, which were formed on the surfaces of high-nitrogen austenitic stainless steels (HNSS) in 0.5 mol/L NaCl solution. The results showed that the HNSS with higher nitrogen content had a larger proportion of low-angle grain boundaries, and it also had a lower corrosion current density in 0.5 mol/L NaCl solution and thus a lower corrosion rate. The existence of a larger proportion of stable oxides (e.g., Cr₂O₃) in the passive films facilitates the passivation/repassivation process and contributes to the high corrosion resistance of HNSS.

npj Materials Degradation (2023)7:75; <https://doi.org/10.1038/s41529-023-00394-x>

INTRODUCTION

Generally, austenitic stainless steel (ASS) has good corrosion resistance in service environments^{1–4} and mechanical properties^{5,6}. Due to its stable and uniform austenitic structure, it has been widely used in pipeline transportation, construction and chemical industries, and other fields⁷. Without the sacrifice of the corrosion performance and mechanical properties of the ASS, the replacement of Ni with other alloying elements (e.g., nitrogen (N) and manganese (Mn)) has been considered to lower the cost. On the other hand, the minimum usage of Ni can also be beneficial to the saving of global natural resources. Recent work showed that austenitic stabilizing elements like N and Mn can be used as substitutes^{8–10}. This facilitates the design and development of ASS possessing a high content of Mn, N, or Cr element and having a low cost^{11–14}, which is considered to be one of the important candidates to replace ASS with a high Ni content (i.e., 8–10 wt.%)¹⁵. Previous work¹⁶ showed that the addition of alloying element N into ASSs would decrease a tendency of pitting corrosion in chloride solutions. This is attributed to the improvement in the protective ability of the passive film formed on the surface of ASS¹⁷.

Many studies showed that the corrosion performance of the ASS is closely related to the N content and the existence status of nitrogen (i.e., whether N is bonding with other elements (i.e., Cr) to form intermetallic nitride). When the N content is low (i.e., less than 0.3 wt.%), the corrosion resistance of ASSs is relatively inferior. Because of the low N content, the number of the C_xN phase in ASS is reduced, triggering that a dense nitride film could barely be formed on the surface¹⁸. When the N content is higher than 0.4 wt.%, the corrosion properties of ASS will be significantly improved¹⁹. For ASSs with high N content, a dense nitride layer could form on the surface. It prevents the oxide film from peeling and has higher corrosion resistance. Therefore, the addition of N in ASSs with high corrosion resistance and low cost has attracted widespread attention and gained great favor²⁰.

As a trace element, N can significantly improve the corrosion resistance of ASS. The N atoms are much smaller in size than the Cr atoms; thus, they can penetrate into the lattice more easily, forming stable nitrides (Cr₂N). The presence of nitrides can deteriorate the corrosion of stainless steel in corrosive media, thereby improving its corrosion resistance. It is reported that the addition of N in the Mn-containing ASS promotes the formation of austenite, expands the composition or temperature range of the austenitic phase and thus inhibits the formation of ferrite^{21–23}. Moreover, N is beneficial to the refinement of the austenitic grains^{24–26} and the mechanical properties of ASS. On the other hand, the N-alloying can improve the resistance to localized corrosion, especially the pitting and intergranular corrosion. The results obtained by Mudali et al.²⁷ showed that increasing the N content in austenitic stainless steel decreased the passive current density, expanded the passive potential range and increased the resistance to intergranular corrosion. The addition of Mn in ASS can strengthen the austenitic lattice, inhibit the formation of residual austenite and increase the stability of ASS. But the study of Toor et al.²⁸ showed that the addition of Mn can deteriorate the corrosion resistance of ASS by lowering the pitting potential and triggering metastable pitting events. It suggests that the addition of a certain content of Mn into austenitic stainless steel has an adverse effect on its corrosion performance. Adding a certain content of Mn into austenitic stainless steel promotes the formation of MnS inclusions, which were preferentially attacked or/and dissolved in the corrosive media, leading to the occurrence of localized corrosion²⁹. Adding an appropriate content of N (i.e., larger than 0.5 wt.%) can not only reduce the grain size and increase the density of Σ3 grain boundaries but also enhance the passivation/repassivation ability and hence promote the resistance to intergranular corrosion and stress cracking corrosion³⁰. Even if severe pitting corrosion with “lace cover” features occurred, the increase of N content to stainless steel could evoke the passivation/repassivation process and increase the pitting corrosion resistance^{31,32}. Therefore, further investigation needs to be conducted to address the effect of N (with the content

¹School of Materials Science and Engineering, Jiangsu University of Science and Technology, 212003 Zhenjiang, China. ²Department of Chemistry, Western University, London, Ontario N6A 5B7, Canada. ³Institute of New Materials, Guangdong Academy of Sciences, National Engineering Research Center of Powder Metallurgy of Titanium & Rare Metals, Guangdong Provincial Key Laboratory of Metal Toughening Technology and Application, 510650 Guangzhou, China. ⁴CAS Key Laboratory of Nuclear Materials and Safety Assessment, Institute of Metal Research, Chinese Academy of Sciences, 110016 Shenyang, China. ✉email: yxqiao@just.edu.cn; jchen496@uwo.ca; zbzheng712003@163.com

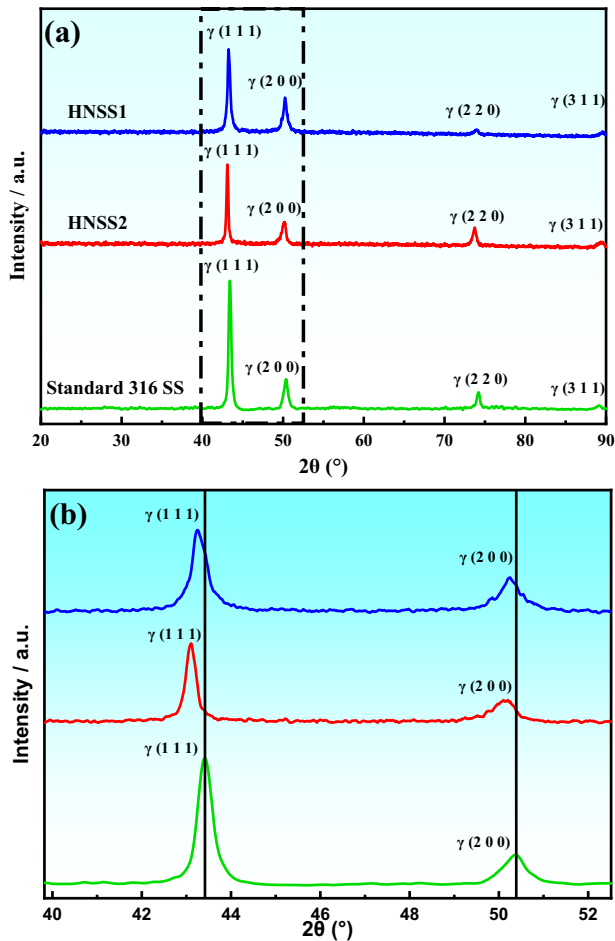


Fig. 1 XRD patterns of the two tested HNSSs and 316 SS. **a** XRD patterns; **b** high magnification of black rectangle in (a) at 2θ range from 42° to 52° .

exceeding 0.5 wt.%) on the passive behaviors of the modified stainless steels, with Ni completely replaced with Mn and N, and the evolution of the composition and structure of the passive films. These studies will help to better understand how Mn and N synergistically function to the formation of a protective layer on the surface of austenitic stainless steel, which can effectively suppress the occurrence of localized corrosion (e.g., intergranular corrosion and stress cracking corrosion³³). These would eventually be beneficial to obtain the optimizing contents of Mn and N in ASS with promising mechanical properties and good corrosion resistance.

In this study, the corrosion behaviors of the HNSS containing ~20 wt.% Mn and various N contents in 0.5 mol/L NaCl solution were investigated by electrochemical impedance spectroscopy, potentiodynamic polarization, scanning electron microscopy and electron backscatter diffraction. In order to evaluate the protective ability of the passive films and characterize the compositions, potentiostatic polarization, Mott-Schottky curve and X-ray photoelectron spectroscopy (XPS) were performed. The aim of the present work was to investigate the effect of N content on the composition and structure of the passive films formed on the surface of the HNSS containing a high Mn content (i.e., 20 wt.%) and influenced its passivation/repassivation process, and to provide guidance on the design of the HNSS with higher corrosion resistance and low cost.

RESULTS AND DISCUSSION

Microstructural features

Figure 1 shows the XRD patterns of the two HNSSs and 316 stainless steel (SS). As seen in Fig. 1a, the diffraction peaks correspond to the γ phase with an FCC structure (standard card number 52-0512), mainly including $\gamma(111)$, $\gamma(200)$, $\gamma(220)$ and $\gamma(311)$. However, a difference exists in peak position and peak intensity, as shown in Fig. 1b. Compared with the result of the 316 SS, the $\gamma(111)$ diffraction peaks of the HNSS1 and HNSS2 slightly shift to a lower angle. It might be relevant to the differences in the contents of alloying elements in these alloys since the incorporation of the alloying element having a smaller or larger atomic radius would result in the atomic arrangement, leading to lattice distortion³⁴. Fujii et al.³⁵ reported that only a small amount of Mn addition increased the f.c.c. lattice constant of CoCrCuFeMnNi because Mn has a large atomic radius. The slightly higher Mn content in the HNSS2 would lead to the shift of the characteristic peak to a lower angle.

Figure 2 presents the microstructure of the two HNSSs. Both of them exhibited a single austenitic phase with twins located inside the austenitic grains. It is clear that the grain size of the HNSS1 (~23.3 μm) is larger than that of the HNSS2 (~8.8 μm). Plenty of voids can be observed inside and at the grain boundaries in the HNSS2, with white inclusions remaining in the voids, as shown in Fig. 2c, d. The inclusions were analyzed using EDS, and the results are shown in Fig. 2e. These inclusions mainly consist of Cr, Fe, Mn, Mo, O and C. It can be inferred that these inclusions are carbides and oxides, which may be produced during the smelting process¹⁷. It is consistent with the results reported by Qin et al.³⁶ that ASS with an N content higher than 0.3 wt.% is prone to produce carbide and oxide inclusions during the smelting process^{37–39}. These inclusions are unable to be detected by XRD because of their low contents. The precipitation of carbide and oxide inclusions on the corrosion properties of the HNSS2 will be detailed discussed in the latter.

The microstructure of 316 SS was characterized and presented in Fig. 3. In Fig. 3a, 316 SS has a granular structure composed of equiaxed austenitic grains with twins distributing inside austenitic grains^{38,39}. Compared to the HNSS1 and HNSS2, these austenitic grains are smaller (Fig. 3b), with an average grain size of 6.1 μm .

EBSD analysis

Figure 4a, b shows the IPF diagrams of the two HNSSs. It can be clearly seen that the HNSS1 is mostly composed of regular polygonal austenitic grains, but the HNSS2 consists of irregular austenitic grains. The grain size distribution results of these two HNSSs are quite different from each other. As shown in Fig. 4c, over 90% of the grains in the HNSS1 possess a grain size smaller than 15 μm , while the grains in the HNSS2 are generally coarse, with the grain size ranges from 5 to 70 μm , as shown in Fig. 4d. The larger proportion of smaller grains with the size smaller than 15 μm is correlated with the increase in content of N, which facilitates the occurrence of partial recrystallization⁴⁰. The grain size difference might lead to the difference in corrosion performance for these two HNSSs.

Figure 4e, f provides Kernel average misorientation diagrams of the two HNSSs. It is clear that there are almost no residual strains in the HNSS1, but there are some residual strains distributing along the grain boundaries, especially at the places where recrystallization occurred. Although the austenitic grains are much less uniform in the HNSS2 than in the HNSS1, but the proportion of small angle grain boundary ($<10^\circ$) in the HNSS2 is much higher, as shown in Fig. 4g, h. The dislocation density of the HNSS1 is smaller than that of the HNSS2 due to the presence of a larger angle grain boundary which can absorb dislocation energy and reduce dislocation density. An⁴¹ reported that the large-angle grain boundary is easy to absorb lattice defects. In addition, the

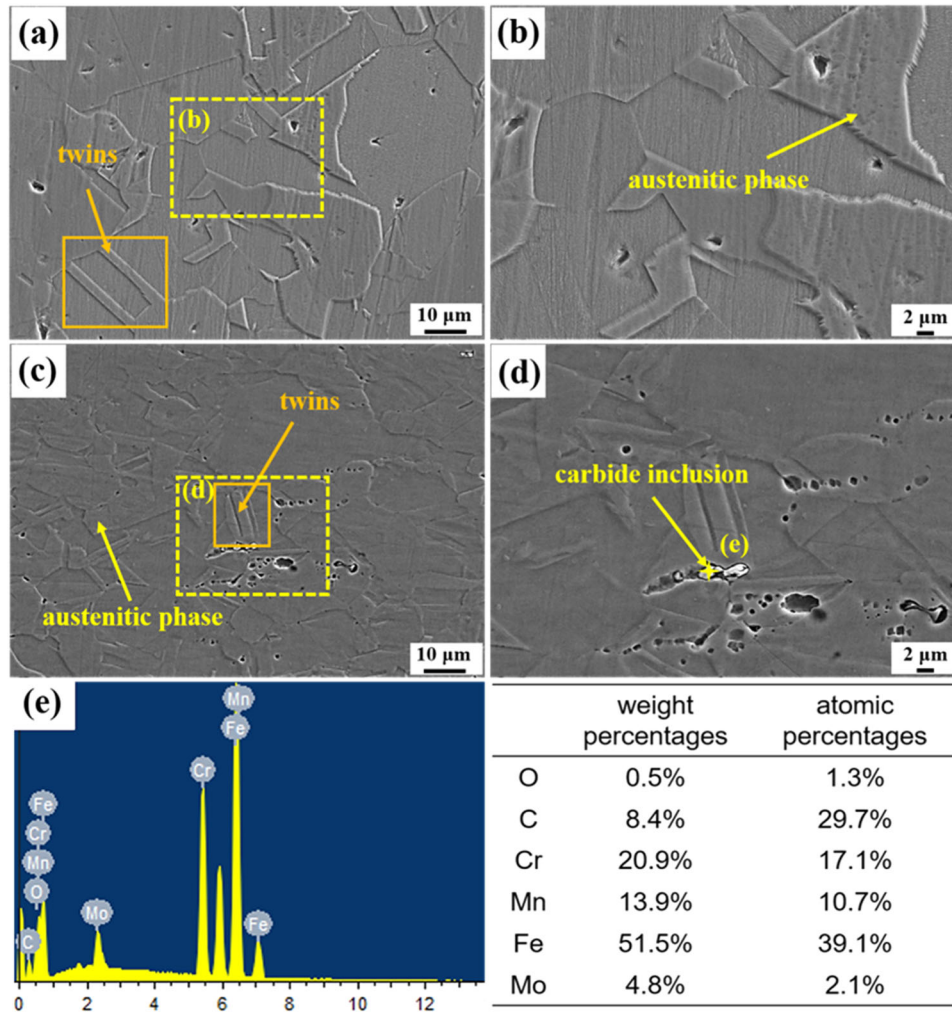


Fig. 2 SEM microstructure and EDS analysis of HNSSs. a, b Microstructure of HNSS1; **c, d** microstructure of HNSS2; **e** EDS analysis of HNSS2.

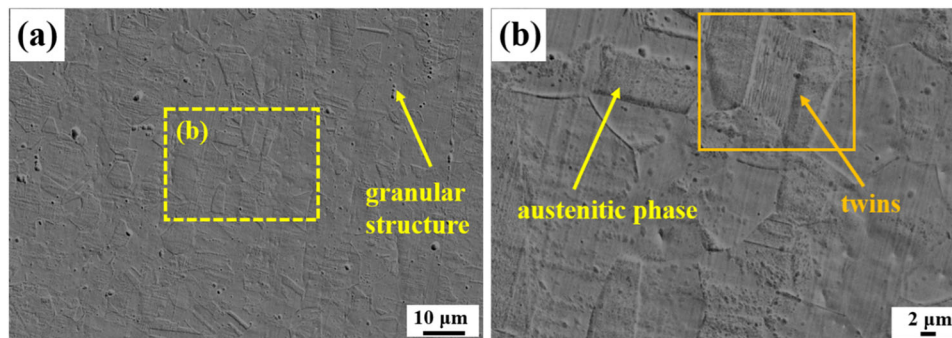


Fig. 3 SEM microstructure of 316 SS. a high magnification; **b** high magnification the rectangular in (a).

small angle boundary will inhibit the low energy segment connected by the large-angle grain boundary network and prevent the corrosion crack from expanding with the high-angle grain boundary⁴², and thus decrease the corrosion tendency.

Electrochemical tests

Figure 5a shows the potentiodynamic polarization of the two HNSSs in 0.5 mol/L NaCl solution. The two HNSSs exhibited a spontaneous passivation behavior, but the passive potential range

of the HNSS1 was narrower than that of the HNSS2. A sudden increase of current density was observed at 0.05 V_{SCE} for the HNSS1, indicating the breakdown of passive film and the occurrence of pitting corrosion. The enlarged view of Fig. 5a, as shown in Fig. 5b, presents current density fluctuations, indicating the initiation and repassivation of metastable pitting. This corrosion feature is frequently observed in potentiodynamic polarization curves of N-containing stainless steels in NaCl solutions⁴³. In contrast, the HNSS2 had a higher pitting corrosion resistance with a wide passive region ranging from about -0.1 to

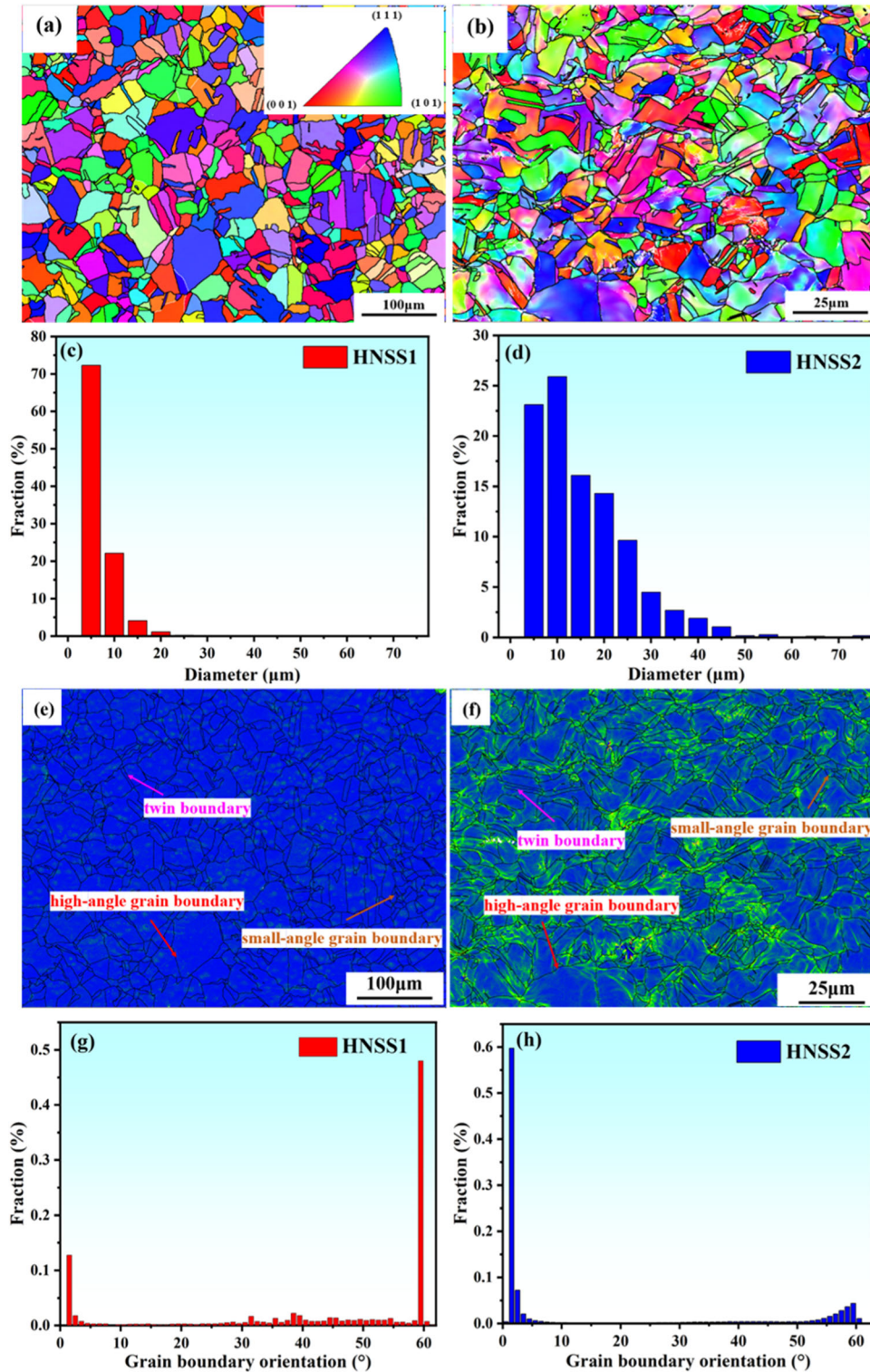


Fig. 4 EBSD of the two tested HNSSs. IPF of **a** HNSS1 and **b** HNSS2; grain size distribution of **c** HNSS1 and **d** HNSS2; Kernel average misorientation figures of **e** HNSS1 and **f** HNSS2; grain boundary orientation of **g** HNSS1 and **h** HNSS2.

1.05 V_{SCE} . Different from HNSS1, HNSS2 has a broader passive potential range up to $\sim 1.05 V_{SCE}$. No current fluctuations can be observed in the potentiodynamic polarization curve of the HNSS2. The electrochemical parameters derived from polarization curves, including the corrosion potential (E_{corr}), corrosion current density (i_{corr}) and pitting potential (E_p), are shown in Table 1. It can be seen that the E_{corr} of the HNSS2 was 70 mV higher than that of the

HNSS1. The i_{corr} of HNSS1 was $5.77 \times 10^{-8} \text{ A cm}^{-2}$, and the i_{corr} of HNSS2 was $4.77 \times 10^{-8} \text{ A cm}^{-2}$. It suggests that the increase of N content improved the pitting resistance of HNSS and is consistent with the results reported by the available literature^{21,44}.

The surface morphologies of the two HNSSs after the potentiodynamic polarization measurements are shown in Fig. 6. From Fig. 6a, a₁, c, and c₁, the corrosion pits appeared on the

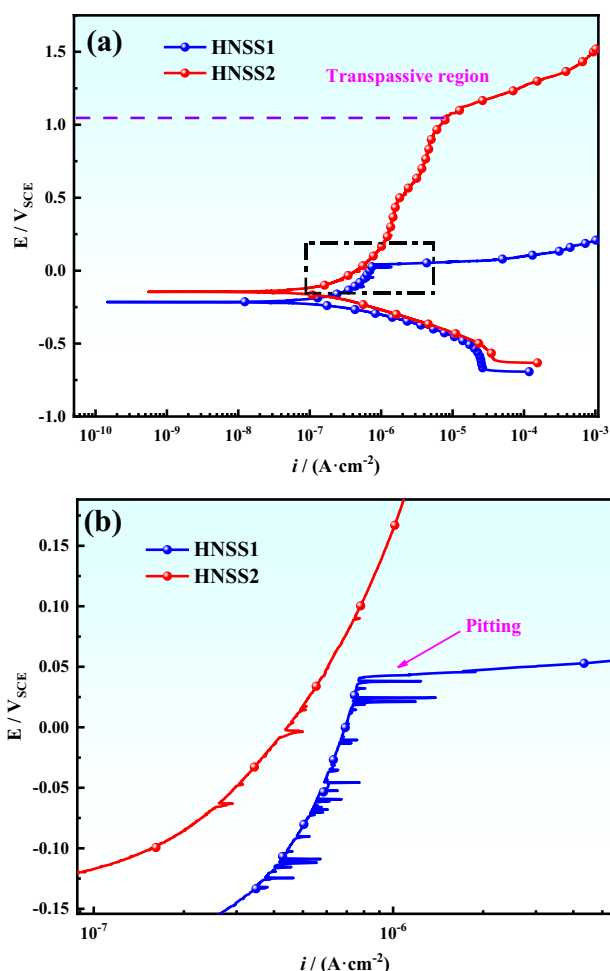


Fig. 5 Potentiodynamic polarization curves of the two HNSSs in 0.5 mol/L NaCl solution. **a** Potentiodynamic polarization; **b** Enlarged view of the black dashed box in (a).

Table 1. Electrochemical parameters derived from potentiodynamic polarization curves in Fig. 5.

	E_{corr} / V_{SCE}	$i_{corr} / A \text{ cm}^{-2}$	E_p / V_{SCE}
HNSS1	-0.22 ± 0.02	$(5.77 \pm 0.12) \times 10^{-8}$	0.05 ± 0.01
HNSS2	-0.15 ± 0.01	$(4.77 \pm 0.14) \times 10^{-8}$	~

surface of both two materials. The number of corrosion pits is much larger for the HNSS1. It can be seen that the HNSS2 has a higher resistance to pitting corrosion. Figure 6b shows that pitting occurring on the surface of HNSS1 has a feature of lacy cover because the oxide inclusions at the surface provide initiation sites for the pits, and the detachment of the inclusions provides positions for the stagnation of the chloride solution, leading to the growth of the pits and the appearance of the lace covers⁴⁵. Similarly, plenty of dense pits were also observed on the surface of HNSS2 in Fig. 6d. There are some minor defects on the surface of HNSS, including casting defects, which can promote the formation of corrosion pits.

Electrochemical impedance spectroscopy (EIS) measurements of HNSS1 and HNSS2 were performed and shown in Fig. 7. From Fig. 7a, the semi-capacitive arcs of the two steels appear in the Nyquist plots, suggesting the domination of a similar corrosion

mechanism^{46,47}. This characteristic was similar to the results of Fe-18Cr-15Mn-0.66 N⁴⁸ and Fe-18Cr-15Mn-2Mo-0.66 N⁴⁹ in a 3.5% NaCl solution. The capacitive arc radius of HNSS1 was smaller than that of HNSS2, suggesting the better corrosion resistance of the HNSS2⁵⁰. These results were in accordance with the corrosion behavior results of Fe-20Cr-20Mn-2.2Mo⁴² alloy in NaCl solution, which showed that increasing the nitrogen content enhanced the protectiveness of the passive film effectively.

In Bode plots (Fig. 7b), phase angles were close to 0° at the frequency of 10⁴ Hz for both HNSSs, indicating that the impedance was solution resistance⁵¹. At the frequency region between 0.1 to 100 Hz, phase angles were close to 80°, suggesting the formation of stable and dense passive films⁵². At the lowest frequency limit (namely 10⁻² Hz), the impedance resistance of HNSS2 was larger than that of HNSS1, indicating that HNSS2 had a higher corrosion resistance. It is in accordance with the potentiodynamic polarization results.

The equivalent circuit used to fitting the EIS spectra in Fig. 7 is shown in Fig. 8. In which R_s is solution resistance, R_f is the resistance of passive film, and CPE is constant phase element representing the capacitance of passive film⁵³. CPE can be described using two parameters: Q and n , where Q is a constant, and n is a variable parameter ranging from 0 to 1 ($n = 1$ means the CPE is a pure capacitor, while $n = 0$ means it is a pure resistance⁵⁴). EIS fitting results were presented in Table 2, yielding that the values of polarization resistance (R_p) were the values of film resistance (R_f). The reciprocal of R_p is proportional to the corrosion rate. At a higher N content, the R_p value was larger, indicating a higher protective ability of passive film and a lower corrosion rate⁵⁵. It is in accordance with the results conducted by Wu et al.⁵⁶ that the addition of N improved the stability of passive film and thus enhanced the passivation of austenitic steel.

The thickness of passive film can be calculated using the equations written below:

$$C_0 = Q_n^{\frac{1}{n}} \cdot R_p^{(1-n)n} \quad (1)$$

$$C_0 = \frac{\epsilon \epsilon_0 A}{d_{ox}} \quad (2)$$

in which C_0 is the capacitance of passive film, R_p is polarization resistance and ϵ the dielectric constant (15.6 for stainless steel⁵⁷), ϵ_0 is the dielectric constant of vacuum ($8.85 \times 10^{-14} \text{ F cm}^{-1}$), A is the area of the sample, and d_{ox} is the thickness of passive film. Although HNSS2 had higher corrosion resistance than HNSS1, the thickness of the passive film was close to each other. The thickness of passive film on the surface of HNSS1 and HNSS2 was 12.7 nm and 13.5 nm, respectively.

Potentiostatic polarization tests

On the basis of the potentiodynamic polarization measurements in Fig. 5, both austenitic steels will be passive at an applied potential of -50 mV_{SCE} . To form a layer of passive film on the surfaces of two HNSSs and to investigate their passivation behavior, potentiostatic polarization tests were performed at this potential for 1 h in 0.5 mol/L NaCl solution. The response of current density (i) with time (t) was plotted in Fig. 9a. It is clear that rapid nucleation and growth of passive films led to the dramatic decrease of the current densities at the initial stage (i.e., $\leq 300 \text{ s}$). As the duration of exposure time increased, the current densities gradually decreased and tended to stabilize at $\sim 10^{-7} \text{ A cm}^{-2}$, indicating the formation of stable passive films. From Fig. 9a, it can be seen that the steady-state current density value of HNSS1 is $1.11 \times 10^{-7} \text{ A cm}^{-2}$, and the steady-state current density value of HNSS2 is $1.52 \times 10^{-7} \text{ A cm}^{-2}$. Lu et al.⁵⁸ found that the lower the current density, the more stable the passive film is. Therefore, the passive film formed on the surface of HNSS2 is more stable and has a higher protective ability on the substrate than HNSS1.

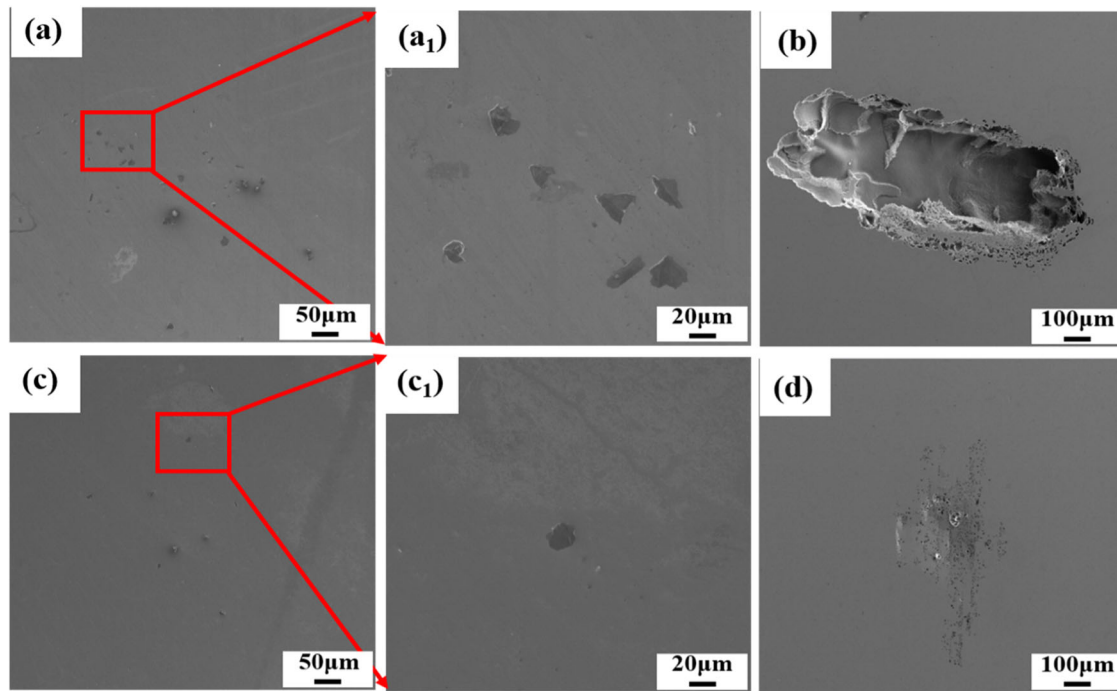


Fig. 6 Corrosion morphologies of the two HNSSs after potentiodynamic polarization test in 0.5 mol/L NaCl solution. **a, a1, b** HNSS1; **c, c1, d** HNSS2.

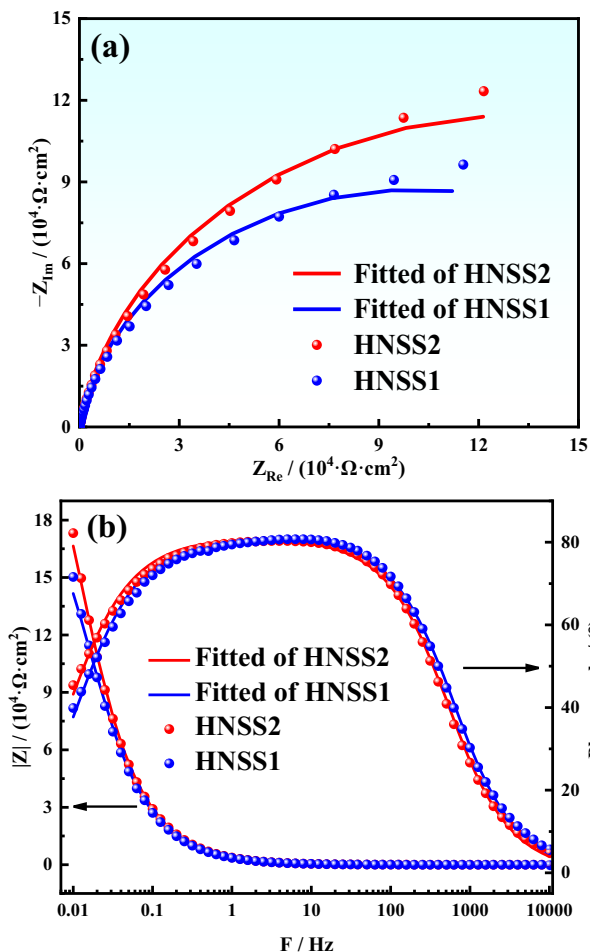


Fig. 7 EIS of HNSS1 and HNSS2 obtained in 0.5 mol/L NaCl solution. **a** Nyquist plots, **b** Bode plots.

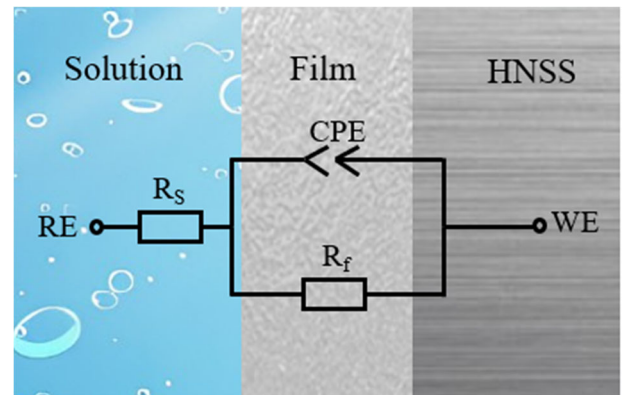


Fig. 8 Schematic of equivalent circuit used to fit EIS present in Fig. 7.

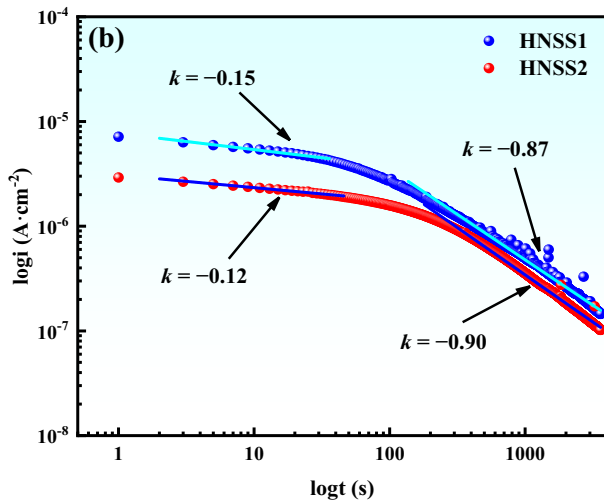
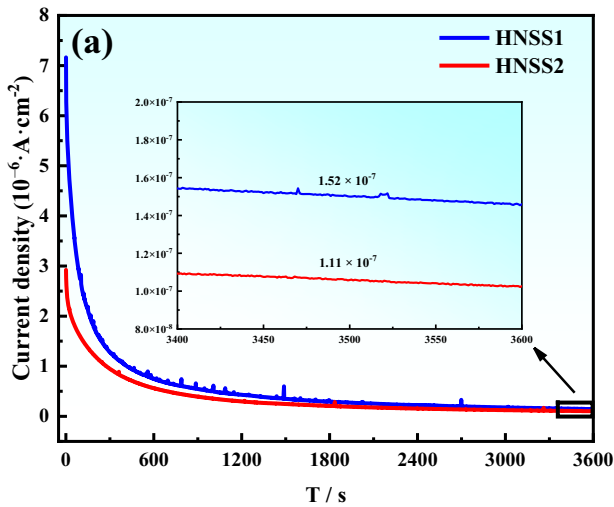
The relationship between i and t can be described as below:

$$i = 10^{-(A+kt)} \quad (3)$$

where A is a constant. k represents the growth rate of the passive film⁴⁶. Figure 9b shows the $\log i$ - $\log t$ plots of two steels. According to the ref.⁵⁹, the growth of the passive film is controlled by electric field. As shown in Fig. 8b, the k values of HNSS1 and HNSS2 were -0.15 and -0.12 at the initial stage (less than 40 s), suggesting that the films formed on these two HNSSs were similar to each other. With the increase of the exposure time, both k values decreased to -0.87 (for the HNSS1) and -0.90 (for the HNSS2). It indicates that passive films formed under these conditions were compact and dense. A lower k value for HNSS2 suggests that the passive film was denser and more compact than the HNSS1 and also had a faster formation rate. The current transient during potentiostatic polarization reflects the initiation and annihilation of the metastable pitting corrosion. There are two types of current transient for the HNSS1, as shown in Fig. 10. The first one showed that the current density increased

Table 2. EIS fitting results of HNSS1 and HNSS2.

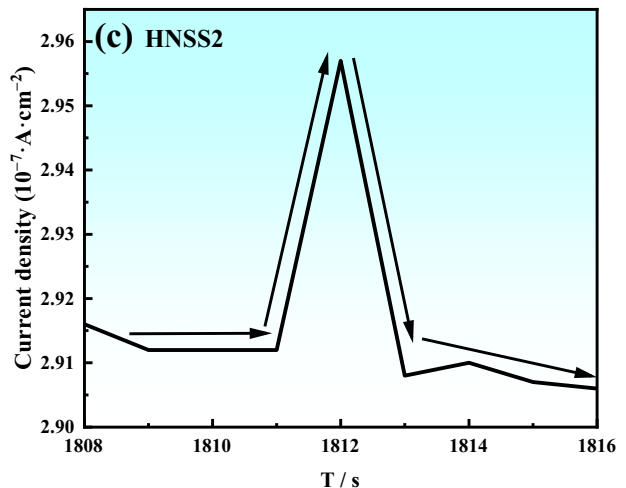
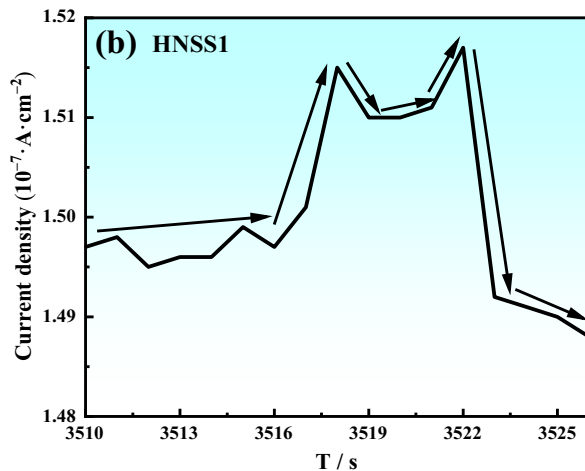
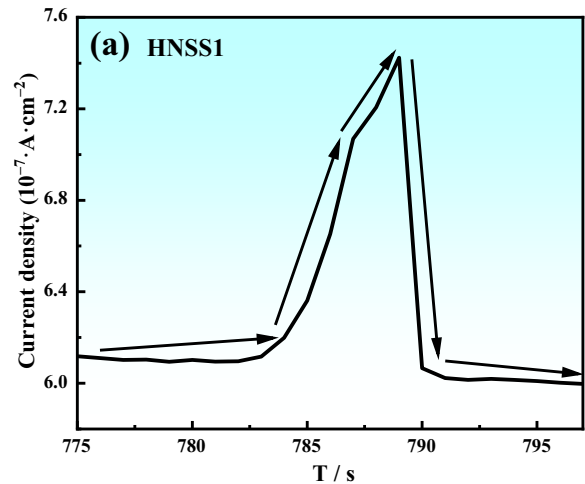
	$R_s / \Omega \text{ cm}^2$	$Q / \Omega^{-1} \text{ s}^n \text{ cm}^{-2}$	n	$R_f / \Omega \text{ cm}^2$	$d_{\text{ox}} / \text{nm}$
HNSS1	10.36 ± 0.05	$(5.34 \pm 0.15) \times 10^{-5}$	0.90	$(1.50 \pm 0.10) \times 10^5$	12.7
HNSS2	12.21 ± 0.05	$(5.55 \pm 0.10) \times 10^{-5}$	0.87	$(1.73 \pm 0.08) \times 10^5$	13.5

**Fig. 9** Current-time response of the two tested HNSSs polarized at -50 mV SCE in 0.5 mol/L NaCl solution. **a** $i-t$ plots; **b** $\log i-\log t$ plots.

quickly in 3 s and then decayed rapidly due to the repassivation process (Fig. 10a), while the other was that the current density surged owing to initially to nucleate the metastable pit, then partially decayed since the initiated metastable pit attempted to re-passive⁶⁰, rose again due to the incomplete repassivation and the propagation of the metastable pit⁶¹, and finally decreased as a consequence of repassivation of the metastable pitting (Fig. 10b). As for the HNSS2, the current density exhibits a transient surge suggesting the event of occurrence metastable pitting, then symmetrically subsided to the background due to the repassivation of passive film⁶², as shown in Fig. 10c.

Nucleation mechanism of the passive film

For passive films with semiconducting properties, such as Fe, Ni, etc., the nucleation and growth processes determined the

**Fig. 10** Typical transient current density peaks showing nucleation and repassivation of metastable pits. **a**, **b** HNSS1; **c** HNSS2.

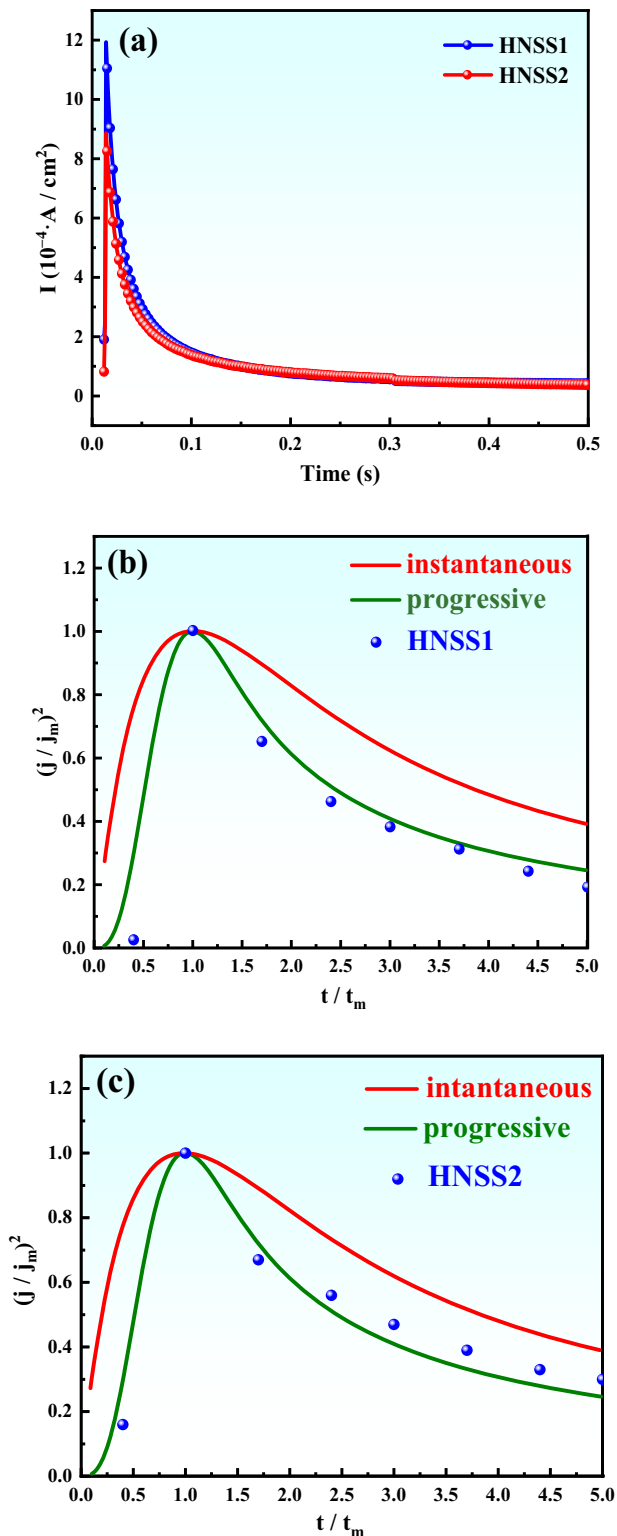


Fig. 11 Current-time response of the two tested HNSSs. **a** Current (i_m) and corresponding time (t_m); experimental and standard nucleation curves of passive film on **b** HNSS1 **c** HNSS2.

permeation speed of point defects through the film, which affects the properties of the passive film⁶³. Figure 11a shows potentiostatic polarization curves of two HNSSs at $-0.05 V_{SCE}$. The current rises in the initial stage of the curve owing to the electrode system to the voltage and then gradually decreases in the response of the

nucleation of passive film. Compared with HNSS1, the current transient of HNSS2 drops faster, implying that the passive film of HNSS2 is better than that of HNSS1⁶⁴. The transient current-time curves obtained from the experiment are transformed accordingly and then compared with the two standard nucleation theory model curves.

$$\frac{j^2}{j_m^2} = \frac{t}{t_m} \left\{ 1 - \exp \left[-2.3367 \left(\frac{t}{t_m} \right)^2 \right] \right\}^2 \quad (4)$$

$$\frac{j^2}{j_m^2} = \frac{1.9542}{t/t_m} \left\{ 1 - \exp \left[-1.2564 \left(\frac{t}{t_m} \right) \right] \right\}^2 \quad (5)$$

where j_m and t_m were the current density and time corresponding to the peak position of the curve obtained from the experiment, respectively.

As shown in Fig. 11b, c, the nucleation mechanisms of passive films of HNSS1 and HNSS2 are consistent with the theoretical curves of continuous nucleation. This suggested that the nucleation mechanism of the two HNSSs complies with the continuous nucleation mechanism. In Fig. 11, HNSS2 is closer to transient nucleation as compared to HNSS1, showing that the active sites on the surface of HNSS2 are rapidly activated during potentiostatic polarization process⁶⁵, which is conducive to the accelerated formation of passive films.

Mott-Schottky analysis

The density of defect or carrier present in passive film is one of the important factors influencing the corrosion performance of passive materials in environments. It can be characterized by the measurement of capacitance (C_{SC}) of the space charge layer as a function of applied potential (E).

Mott-Schottky equations are usually used to describe the correlation of capacitance of the space charge layer with applied potential, which is given for n-type/p-type semiconductor as follows⁶⁶:

$$\frac{1}{C_{SC}^2} = \frac{2}{\epsilon \epsilon_0 e N_D} \left(E - E_{fb} - \frac{kT}{e} \right) \text{ for n-type semiconductor} \quad (6)$$

$$\frac{1}{C_{SC}^2} = \frac{2}{\epsilon \epsilon_0 e N_A} \left(E - E_{fb} - \frac{kT}{e} \right) \text{ for p-type semiconductor} \quad (7)$$

where ϵ is the dielectric constant of passive film, ϵ_0 is vacuum permittivity constant ($8.854 \times 10^{-14} \text{ F}\cdot\text{cm}^{-1}$), e is electron charge ($1.6021 \times 10^{-19} \text{ C}$), N_D and N_A are donor and acceptor density, respectively, E_{fb} is flat-band potential, k is Boltzmann constant ($1.38 \times 10^{-23} \text{ J}\cdot\text{K}^{-1}$), and T is temperature (K).

Figure 12 shows Mott-Schottky curves of two HNSSs in 0.5 mol/L NaCl solution. It can be said that the Mott-Schottky curves had the feature of an n-p type semiconductor. The slopes of the linear parts in region I and region II were fitted to calculate the donor and acceptor densities in passive film. As is seen in Table 3, the donor density in passive film in region I for HNSS1 and HNSS2 was $1.09 \times 10^{21} \text{ cm}^{-3}$ and $0.85 \times 10^{21} \text{ cm}^{-3}$, respectively. The acceptor density in region II was $2.55 \times 10^{21} \text{ cm}^{-3}$ and $2.24 \times 10^{21} \text{ cm}^{-3}$, respectively. The lower donor/acceptor density in passive film formed on the surface of HNSS2 suggests higher corrosion resistance.

Passive film characterization

Figure 13 shows the XPS spectra of passive films formed on the surfaces of the two HNSSs. The results showed that passive films were composed of Fe, Mn, Cr, O, N and C elements. Although nitrogen contents were different in these two HNSSs, the similar peak intensities of these elements showed that the contents of these elements present in passive films were similar. Figure 14a,

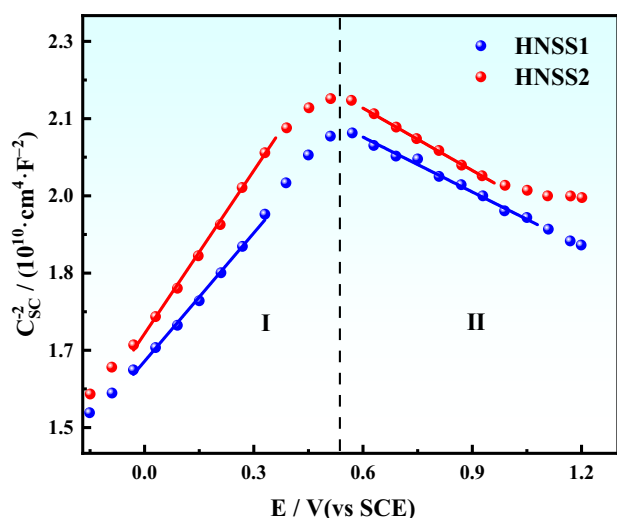


Fig. 12 Mott-Schottky plots of the two tested HNSSs in 0.5 mol/L NaCl solution.

	N_D (cm^{-3})	N_A (cm^{-3})
HNSS1	1.09×10^{21}	2.55×10^{21}
HNSS2	0.85×10^{21}	2.24×10^{21}

b shows Fe 2p_{3/2} high-resolution XPS for passive films formed on the surfaces of the two HNSSs. Both of the two spectra are comprised of peaks of metallic Fe⁰ (707.8 eV), Fe₃O₄ (708.9 eV), Fe₂O₃ (710.4 eV) and FeOOH (712.3 eV)⁶⁷. The fraction of these substances can be obtained by XPS fitting, as shown in Fig. 15a. It is shown that the fraction of metallic Fe⁰ in HNSS2 is less than that in HNSS1, while the fraction of Fe₃O₄, Fe₂O₃ and FeOOH in HNSS2 is higher. It seemed that higher N may induce the formation of a higher proportion of Fe_xO_y in passive film, which enhances the protective ability of passive film and increases corrosion resistance. Feng⁶⁸ found that with the increase of N content, the fraction of Fe₃O₄ and Fe₂O₃ gradually increased, the fraction of metallic Fe⁰ decreased, the defect concentration of passive film was low, and the protection performance was better.

Figure 14c and d are Cr 2p_{3/2} spectra for passive films formed on the surfaces of the two HNSSs. The peaks can be identified as metallic Cr⁰ (574.2 eV), Cr₂O₃ (576.1 eV) and Cr(OH)₃ (578.1 eV). The content of metallic Cr⁰ and Cr(OH)₃ in HNSS1 is low, while the fraction of Cr₂O₃ in HNSS2 is high, as shown in Fig. 15b. The Cr₂O₃/Cr(OH)₃ value of HNSS1 is 0.81, while that of HNSS2 surface increased to 0.99. Compared with Cr(OH)₃, the Cr₂O₃ has lower point defect density and higher thermodynamic stability. Li et al.⁶⁹ reported that the higher the fraction of Cr₂O₃ in passive film, the stronger the protective ability. Therefore, the higher the Cr₂O₃/Cr(OH)₃ value of HNSS2, the passive film on the surface of HNSS2 (with higher N) exhibited higher stability and good protection ability.

Figure 14e, f are N 1s spectra for passive films formed on the surfaces of the two HNSSs. There are three forms of N element in the passive film, free nitrogen N⁰ (398.6 eV), NH₃ (399.8 eV) and NH₄⁺ (400.8 eV). Sun et al.⁷⁰ reported that the adsorption of NH₃ on the surface of ASS can improve the stability of the passive film. The findings of Wang et al.⁷¹ also showed that the presence of NH₄⁺ and NH₃ originate from the dissolving of N, the

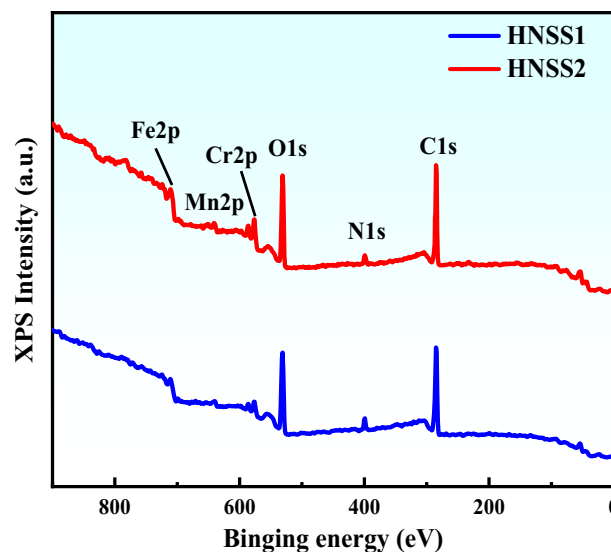


Fig. 13 XPS of passive films formed on the surfaces of the two tested HNSSs.

formation of NH₄⁺ and NH₃ can consume the H⁺, which could promote the repassivation of metastable pits. As shown in Fig. 15c, the NH₄⁺ content of HNSS2 is higher than that of HNSS1, which suggests that the higher N may effectively inhibit the breakdown of passive film and the occurrence of pitting corrosion.

Figure 14g, h are O 1s spectra for passive films formed on HNSS1 and HNSS2. The results showed that the O element in the passive film is composed of O²⁻ (530.2 eV), OH⁻ (532 eV) and H₂O (533.6 eV). The existence of O²⁻ and OH⁻ in the passive film corresponded to metallic oxide and metallic hydroxide, respectively. Figure 15d shows the ratio of O²⁻/OH⁻ in the XPS fitting result for HNSS2 is 0.64, and for HNSS1 is 0.49. Accordingly, the higher ratio of HNSS2 corresponds to the less serious risk of pitting corrosion. Vignal et al.⁷² found that with a significant increase in the O²⁻/OH⁻ ratio, oxide on the surface of passive film formed on the austenite increased, and the passivity of metal was strengthened, which hindered the corrosion rate.

Corrosion mechanism

The corrosion resistance of stainless steel depends on the Cr, which is in the form of Cr₂O₃ on its surface, to ensure that the protective oxide film is self-healing. When the passive film is destroyed by corrosive ions such as Cl⁻, there is enough Cr³⁺ to reform the film. Based on the results obtained, the corrosion mechanism of HNSS in 0.5 mol/L NaCl solution is proposed and is shown in Fig. 16. As shown in Fig. 16, in the Cl⁻ containing environment, the preferential adsorption of Cl⁻ on the surface of HNSS passive film could extruding oxygen atoms, and combining with Fe²⁺ in the passive film to form soluble chloride, resulting in small corrosion pits. In serious cases, there will be a "lace cover". The presence of Cl⁻ directly destroys the passive state of stainless steel. Pitting refers to the localized occurrence of small pits with a certain depth on the surface of HNSS in corrosive environments, which are prone to occur in areas such as oxygen carbide inclusions, secondary phases, grain boundaries, and defects. The published works indicated that the N in metallic material can promote the pitting resistance of HNSS^{16,17}. The preferential enrichment of N due to the anodic segregation could inhibit the dissolution of the matrix and improve the passivity of HNSSs. During the corrosion

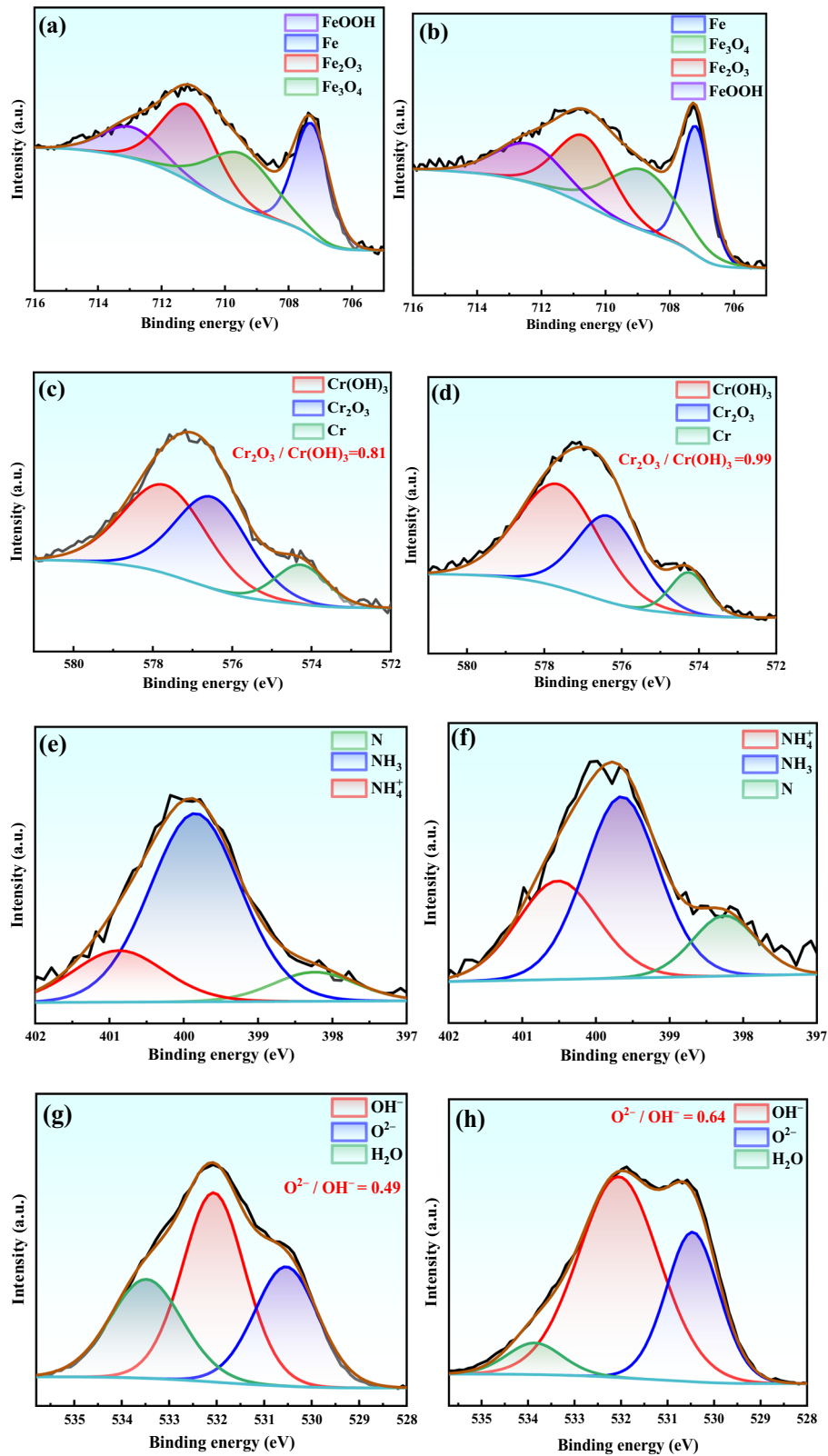


Fig. 14 Detailed element spectra of the passive films formed on the two tested HNSSs. **a, c, e, g** HNSS1; **b, d, f, h** HNSS2; **a, b** Fe2p, **c, d** Cr2p, **e, f** N1s, **g, h** O1s. The black line is the test data and the brown line is the data obtained by CasaXPS peak fitting.

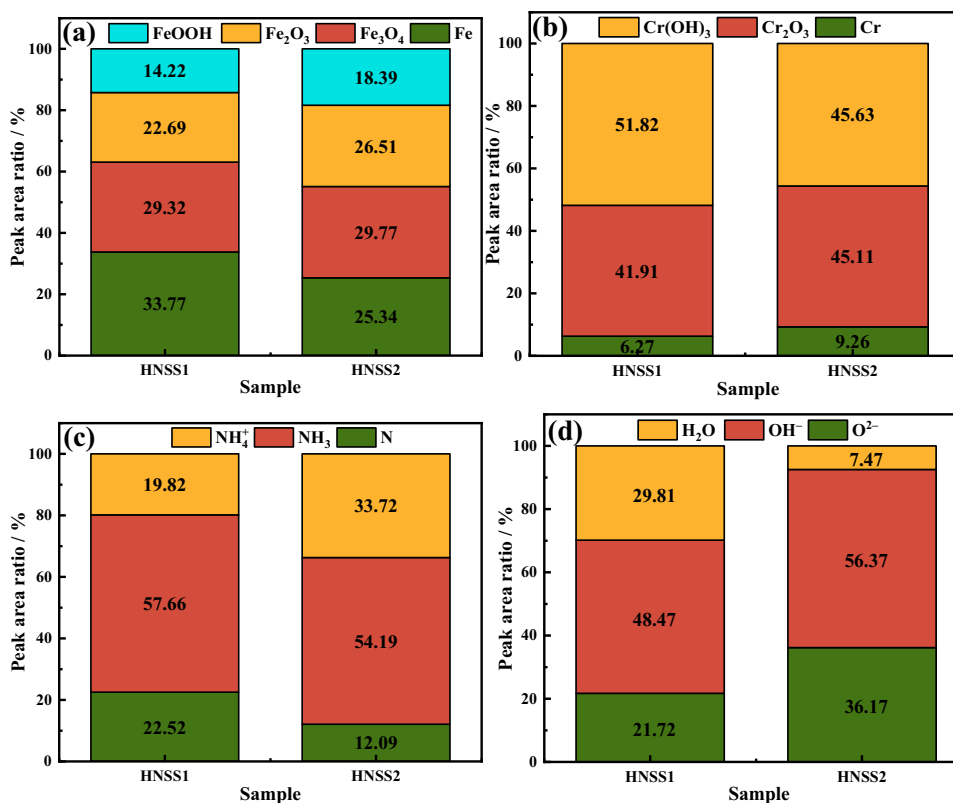


Fig. 15 Percentage of peak area of the element in the passive films. a Fe, b Cr, c N, d O.

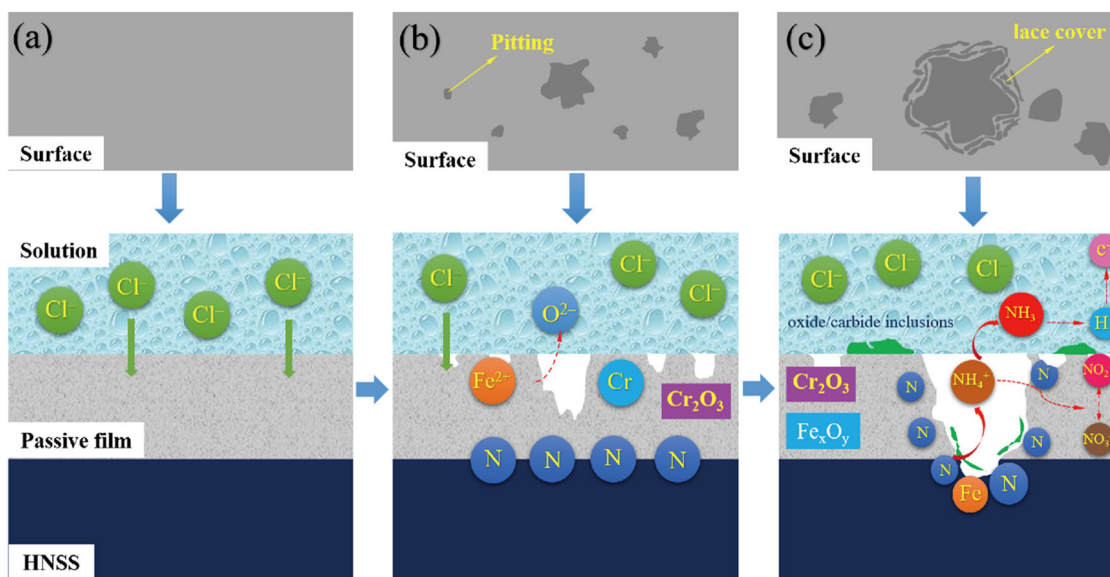


Fig. 16 Corrosion mechanism of HNSS in 0.5 mol/L NaCl. a Preferential adsorption of Cl⁻ on the passive film, b pit grown in HNSS and its lacy cover after potentiodynamic polarization test.

reaction process, N dissolution easily forms NH₃ or NH₄⁺, reducing acidity and promoting passive performance in areas such as pitting and crevice corrosion. Grabke et al.⁷³ reported that N is beneficial to enhance the repassivation ability of HNSS, rapidly promoting the repassivation of the material and inhibiting the growth of pitting corrosion.

The corrosion mechanism of nitrogen on the pitting corrosion process of HNSS is as follows⁷⁴:

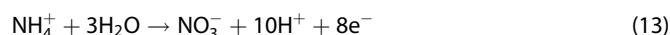
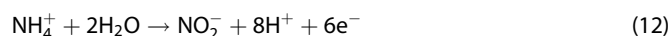
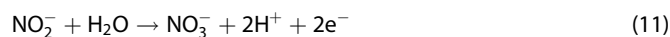
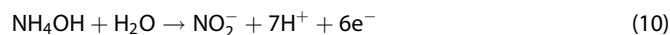


The dissolution of N also forms a dense and protective nitrogen oxide layer while forming NO₃⁻ or NO₂⁻, which serves as a

Table 4. Chemical composition of the tested specimens (in wt.%).

	C	Si	Mn	N	Cr	Mo	S	P	Fe
HNSS1	0.055	0.19	19.50	0.64	19.52	2.24	0.003	≤0.03	Bal.
HNSS2	0.048	0.22	19.68	0.75	19.71	2.23	0.003	≤0.03	Bal.

corrosion inhibitor and can effectively suppress local corrosion.



METHODS

Materials

The materials used in this work were Fe-20Cr-20Mn-0.64N (HNSS1) and Fe-20Cr-20Mn-0.75N (HNSS2) ASS, provided by Northeastern University, China. The compositions of these two ASSs are shown in Table 4. The two HNSSs were cut into coupons with dimensions of 10 × 10 × 2 mm, ground with sandpaper to 1500 #, then polished using 2.5 μm diamond paste, ultrasonically cleaned in ethanol and water, and finally etched using FeCl₃ solution (10 g FeCl₃, 30 mL HCl and 120 mL H₂O) for 15 s. The 316 SS was etched using 10% oxalic acid electrolysis for etching. When preparing the working electrode, connect the copper wire with conductive adhesive on the back of the sample working surface and seal the sample with epoxy resin.

Surface characterization

After etching, the microstructure of the tested steels was observed using a scanning electron microscope (SEM, XL30-FEG ESEM, FEI, Hillsboro, OR, USA). To identify texture, grain size and grain orientation, they were subsequently characterized using back electron scattering diffraction (EBSD). The phases of the HNSSs were identified using a D/Max 2400 X-ray diffractometer (Rigaku Corporation, Tokyo, Japan) with the K_α radiation of Cu at 10 kV and 40 mA. The scan rate of XRD was 6°/min. The surface morphologies of the two HNSSs after the potentiodynamic polarization test were observed using SEM. The samples were potentiostatically polarized at an applied potential of −0.05 V_{SCE} for 1 h and were then analyzed using X-ray photoelectron spectroscopy (ESCALAB 250Xi T) using an Al K_α radiation source, and the results were fitted with CasaXPS peak fitting software.

Electrochemical tests

Electrochemical tests were carried out in a traditional three-electrode system which consisted of the auxiliary electrode of Pt sheet with an exposed area of 40 cm², a reference electrode of saturated calomel electrode (SCE). The electrochemical tests were conducted using Gamry Reference 1010E (Gamry Instruments, Inc. USA) electrochemical workstation.

Prior to potentiodynamic polarization measurements, the samples were monitored at open circuit potentials (OCP) for 3600 s to achieve steady state. The potentiodynamic polarization measured with the scanning potential ranged from −0.5 to 1 V_{SCE} of the (HNSS1) and −0.5 to 1.5 V_{SCE} (HNSS2), with a scanning rate of 20 mV/min. Electrochemical impedance spectroscopy was performed at OCP with the frequency range of 10⁴ ~ 1^{−2} Hz, and

the amplitude is 10 mV. Potentiostatic polarization tests were conducted at a potential of −0.05 V_{SCE} for 3600 s, and then Mott-Schottky tests were performed immediately from −0.6 to 1.2 V_{SCE} at a fixed frequency of 10³ Hz and a scanning rate of 30 mV/s. All electrochemical tests were carried out in 0.5 mol/L NaCl solution at room temperature (25 ± 1 °C). Each experiment was repeated three times to ensure the repeatability.

DATA AVAILABILITY

The data that support the findings of this study are available from Dr. Yanxin Qiao (Email: yxqiao@just.edu.cn) upon reasonable request.

Received: 9 February 2023; Accepted: 12 September 2023;

Published online: 21 September 2023

REFERENCES

- Wang, T. H. et al. Effect of boron on dissolution and repairing behavior of passive film on S31254 super-austenitic stainless steel immersed in H₂SO₄ solution. *J. Iron Steel Res. Int.* **29**, 1012–1025 (2022).
- Pujar, M. G., Kamachi, M. U. & Singh, S. S. Electrochemical noise studies of the effect of nitrogen on pitting corrosion resistance of high nitrogen austenitic stainless steels. *Corros. Sci.* **53**, 4178–4186 (2011).
- Olsson, C. O. A. & Landolt, D. Passive films on stainless steels—chemistry, structure and growth. *Electrochim. Acta* **48**, 1093–1104 (2003).
- Wang, S. et al. Titanium microalloying of steel: a review of its effects on processing, microstructure and mechanical properties. *Int. J. Miner. Metall. Mater.* **29**, 645–661 (2022).
- Qiao, Y. X. et al. Recent progress in microstructural evolution, mechanical and corrosion properties of medium-Mn steel. *J. Iron Steel Res. Int.* **30**, 1463–1476 (2023).
- Talha, M. C., Behera, K. & Sinha, O. P. In-vitro long term and electrochemical corrosion resistance of cold deformed nitrogen containing austenitic stainless steels in simulated body fluid. *Mater. Sci. Eng. C* **40**, 455–466 (2014).
- Poonguzhali, A. M., Pujar, G. & Kamachi, M. U. Effect of nitrogen and sensitization on the microstructure and pitting corrosion behavior of AISI type 316LN stainless steels. *J. Mater. Eng. Perform.* **22**, 1170–1178 (2012).
- Ha, H. Y., Jang, H. J. & Kwon, H. S. Effects of nitrogen on the passivity of Fe-20Cr alloy. *Corros. Sci.* **51**, 48–53 (2009).
- Dalipi, R. et al. Study of metal release from stainless steels in simulated food contact by means of total reflection X-ray fluorescence. *J. Food Eng.* **173**, 85–91 (2016).
- Taiwade, R. V. et al. Effect of grain size on degree of sensitization of chrome-manganese stainless steel. *ISIJ Int.* **53**, 2206–2212 (2013).
- Zambon, A., Ferro, P. & Bonollo, F. Microstructural, compositional and residual stress evaluation of CO₂ laser welded superaustenitic AISI 904L stainless steel. *Mater. Sci. Eng. A* **424**, 117–127 (2006).
- Zhou, Z. L. & Johan, L. Dissimilar welding of super-duplex and super-austenitic stainless steels. *Weld. World* **61**, 21–33 (2016).
- Momeni, A., Dehghani, K. & Keshmiri, H. Hot deformation behavior and microstructural evolution of a superaustenitic stainless steel. *Mater. Sci. Eng. A* **527**, 1605–1611 (2010).
- Lee, C. M., Lee, Y. C. & Lee, C. H. Possibility of Mn substitution of Ni through evaluation of mechanical properties and corrosion resistance in superaustenitic stainless steel weld metal. *Mater. Sci. Eng. A* **733**, 16–23 (2018).
- Cui, B., Zhang, H. & Liu, F. D. Effects of shielding gas composition on the welding stability, microstructure and mechanical properties in laser-arc hybrid welding of high nitrogen steel. *Mater. Res. Express* **5**, 1–17 (2018).
- Ningshen, S., Kamachi, U. M., Mittal, V. K. & Khatak, H. S. Semiconducting and passive film properties of nitrogen-containing type 316LN stainless steels. *Corros. Sci.* **49**, 481–496 (2007).
- Ha, H. Y., Lee, T. H. & Oh, C. S. Effects of combined addition of carbon and nitrogen on pitting corrosion behavior of Fe-18Cr-10Mn alloys. *Scr. Mater.* **61**, 121–124 (2009).
- Diana, L. et al. Effect of nitrogen on the corrosion-erosion synergism in an austenitic stainless steel. *Tribol. Int.* **44**, 610–616 (2011).
- Hanninen, H. E. Applications and performance of high nitrogen steels. *Steel Grips* **2**, 371–380 (2004).
- Lokeswar, P., Saikat, R. M. & Sunil, K. Status of nickel free stainless steel in biomedical field: a review of last 10 years and what else can be done. *Mater. Today. Proc.* **26**, 638–643 (2020).

21. Ningshen, S. et al. Hydrogen effects on the passive film formation and pitting susceptibility of nitrogen containing type 316L stainless steels. *Corros. Sci.* **48**, 1106–1121 (2006).
22. Wu, X. Q. et al. Investigation on pitting corrosion of nickel-free and manganese-alloyed high-nitrogen stainless steels. *J. Mater. Eng. Perform.* **18**, 287–298 (2009).
23. Olefjord, I. & Wegrelius, L. The influence of nitrogen on the passivation of stainless steels. *Corros. Sci.* **38**, 1203–1220 (1996).
24. Yang, K. & Ren, Y. Nickel-free austenitic stainless steels for medical applications. *Sci. Technol. Adv. Mater.* **11**, 014105 (2010).
25. Chen, S. S. et al. High nitrogen stainless steel drug-eluting stent—assessment of pharmacokinetics and preclinical safety in vivo. *Bioact. Mater.* **5**, 779–786 (2020).
26. Hukovic, M. M. et al. High corrosion resistance of austenitic stainless steel alloyed with nitrogen in an acid solution. *Corros. Sci.* **53**, 2176–2183 (2011).
27. Mudali, U., Ningshen, K. S. & Tyagi, A. K. Influence of metallurgical and chemical variables on the pitting corrosion behaviour of nitrogen-bearing austenitic stainless steels. *Mater. Sci. Forum* **318–320**, 495–502 (1999).
28. Toor, I. H. Evaluation of corrosion performance of two Mn-containing stainless steel alloys. *Int. J. Mater. Res.* **105**, 386–391 (2014).
29. Liang, C. H. & Zhang, J. D. Effect of phosphorus, silicon, manganese and copper on the pitting corrosion resistance of high purity 18Cr-14Ni stainless steel in chloride solution. *Corros. Sci. Prot. Technol.* **7**, 336–340 (1995).
30. Tao, X. et al. Evaluation of the sliding wear and corrosion performance of triode-plasma nitrided Fe-17Cr-20Mn-0.5N high-manganese and Fe-19Cr-35Ni-1.2Si high-nickel austenitic stainless steels. *Surf. Coat. Tech.* **409**, 126890 (2021).
31. Qiao, Y. X. et al. Corrosion behavior of a nickel-free high-nitrogen stainless steel with hydrogen charging. *JOM* **73**, 1165–1172 (2021).
32. Fu, Y. et al. Effects of nitrogen on the passivation of nickel-free high nitrogen and manganese stainless steels in acidic chloride solutions. *Electrochim. Acta* **54**, 4005–4014 (2009).
33. Li, J. G. et al. Effects of heat input and cooling rate during welding on intergranular corrosion behavior of high nitrogen austenitic stainless steel welded joints. *Corros. Sci.* **166**, 108445 (2020).
34. Liu, H. F. et al. XRD and EBSD studies of severe shot peening induced martensite transformation and grain refinements in austenitic stainless steel. *Mater. Charact.* **168**, 110574 (2020).
35. Fujii, T., Yamakawa, R. & Tohgo, K. Analysis of the early stage of stress corrosion cracking in austenitic stainless steel by EBSD and XRD. *Mater. Character* **172**, 110882 (2021).
36. Qin, F. M. et al. Effect of nitrogen content on precipitation behavior and mechanical properties of Mn18Cr18N austenitic stainless steel. *Acta Metall. Sin.* **54**, 55–64 (2018).
37. Taylor, C. D. et al. Integrated computational materials engineering of corrosion resistant alloys. *NPJ Mater. Degrad.* **2**, 1–10 (2018).
38. Li, L. et al. Effect of cavitation erosion induced surface damage on the corrosion behavior of TA31 titanium alloy. *Ultrason. Sonochem.* **98**, 106498 (2023).
39. Luo, H., Su, H. Z. & Dong, C. F. Passivation and electrochemical behavior of 316L stainless steel in chlorinated simulated concrete pore solution. *Appl. Surf. Sci.* **400**, 38–48 (2017).
40. Feng, W., Yang, S. & Yan, Y. B. Dependence of grain boundary character distribution on the initial grain size of 304 austenitic stainless steel. *Philos. Mag.* **97**, 1057–1070 (2017).
41. An, S. Y. et al. Effect of grain boundary engineering treatment on corrosion resistance and mechanical properties of 304 stainless steel. *Nonferr. Met. Mater. Eng.* **43**, 19–26 (2021).
42. Shi, F. et al. Application of grain boundary engineering to improve intergranular corrosion resistance in a Fe-Cr-Mn-Mo-N high-nitrogen and nickel-free austenitic stainless steel. *Acta Metal. Sin. (Engl. Lett.)* **33**, 789–798 (2020).
43. Qi, X., Mao, H. H. & Yang, Y. T. Corrosion behavior of nitrogen alloyed martensitic stainless steel in chloride containing solutions. *Corros. Sci.* **120**, 90–98 (2017).
44. Xu, L. W. et al. Effects of nitrogen content on pitting corrosion resistance of non-magnetic drill collar steel. *J. Iron Steel Res. Int.* **27**, 1466–1475 (2020).
45. Kamachi Mudali, U. et al. Pitting corrosion studies on nitrogen bearing austenitic stainless steels. *Mater. Trans.* **37**, 1568–1573 (1996).
46. Liu, L., Li, Y. & Wang, F. H. Influence of nanocrystallization on passive behavior of Ni-based superalloy in acidic solutions. *Electrochim. Acta* **52**, 2392–2400 (2007).
47. Luo, H. et al. Characterization of electrochemical and passive behaviour of Alloy 59 in acid solution. *Electrochim. Acta* **135**, 412–419 (2014).
48. Qiao, Y. X. et al. Effect of aging treatment on microstructure and corrosion behavior of a Fe-18Cr-15Mn-0.66N stainless steel. *J. Mater. Sci. Technol.* **107**, 197–206 (2022).
49. Zhang, H. et al. Microstructural evolution and pitting corrosion behavior of friction stir welded joint of high nitrogen stainless steel. *Mater. Des.* **110**, 802–810 (2016).
50. Qiao, Y. X. et al. Cavitation erosion behaviors of a nickel-free high-nitrogen stainless steel. *Tribol. Lett.* **67**, 1 (2019).
51. Shukla, A. K., Balasubramaniam, R. & Bhargava, S. Properties of passive film formed on CP titanium, Ti-6Al-4V and Ti-13.4Al-29Nb alloys in simulated human body conditions. *Intermetallics* **13**, 631–637 (2005).
52. Wang, Z. B., Hu, H. X. & Liu, C. B. The effect of fluoride ions on the corrosion behavior of pure titanium in 0.05M sulfuric acid. *Electrochim. Acta* **135**, 526–535 (2014).
53. Sotniczuk, A. et al. Corrosion behaviour of biomedical Ti under simulated inflammation: exploring the relevance of grain refinement and crystallographic texture. *Corros. Sci.* **200**, 110238 (2022).
54. Orazem, M. E. et al. Invited interpretation of dielectric properties for materials showing constant phase element CPE impedance response. *J. Electrochem. Soc.* **45**, 15–35 (2013).
55. Feng, H. et al. Sn microalloying enhances corrosion resistance of stainless steel by accelerating heterogeneous nucleation of passive film. *Corros. Sci.* **201**, 110279 (2022).
56. Wu, X. Q. et al. Effects of nitrogen on passivity of nickel-free stainless steels by electrochemical impedance spectroscopy analysis. *J. Mater. Eng. Perform.* **24**, 3607–3614 (2015).
57. Shi, J. J., Zou, Y. Q. & Ming, J. Effect of DC stray current on electrochemical behavior of low-carbon steel and 10%Cr steel in saturated Ca(OH)₂ solution. *Corros. Sci.* **169**, 108610 (2020).
58. Li, L. et al. Effect of cavitation erosion induced surface damage on pitting and passive behaviors of 304L stainless steel. *Int. J. Miner. Metall. Mater.* **30**, 1338–1352 (2023).
59. Gui, Y., Zheng, Z. J. & Gao, Y. The bi-layer structure and the higher compactness of a passive film on nanocrystalline 304 stainless steel. *Thin Solid Films* **599**, 64–71 (2016).
60. Burstein, G. T., Liu, C. & Souto, R. M. The effect of temperature on the nucleation of corrosion pits on titanium in Ringer's physiological solution. *Biomaterials* **26**, 245–256 (2005).
61. Cui, Y. W. et al. Metastable pitting corrosion behavior of laser powder bed fusion produced Ti-6Al-4V in Hank's solution. *Corros. Sci.* **203**, 110333 (2022).
62. Souto, R. M. & Burstein, G. T. A preliminary investigation into the microscopic depassivation of passive titanium implant materials in vitro. *J. Mater. Sci. Technol.* **7**, 337–343 (1996).
63. Gai, X. et al. Electrochemical behaviour of passive film formed on the surface of Ti-6Al-4V alloys fabricated by electron beam melting. *Corros. Sci.* **145**, 80–89 (2018).
64. Tang, Y. M., Zuo, Y. & Zhao, X. H. The metastable pitting behaviors of mild steel in bicarbonate and nitrite solutions containing Cl⁻. *Corros. Sci.* **50**, 989–994 (2008).
65. Zhang, L. J. et al. Study on the anodic film formation process of AZ91D magnesium alloy. *Electrochim. Acta* **52**, 5325–5333 (2007).
66. Gao, S. J. et al. Electrochemical behavior and nonlinear Mott-Schottky characterization of a stainless steel passive film. *Anal. Lett.* **47**, 1162–1181 (2014).
67. Zhu, M., Zhang, Q. & Yuan, Y. F. Passivation behavior of 2507 super duplex stainless steel in simulated concrete pore solution. *J. Mater. Eng. Perform.* **29**, 3141–3151 (2020).
68. Feng, H. et al. Influence of nitrogen on corrosion behaviour of high nitrogen martensitic stainless steels manufactured by pressurized metallurgy. *Corros. Sci.* **144**, 288–300 (2018).
69. Li, J., Wang, Q. C. & Yang, Y. X. Enhancing pitting corrosion resistance of severely cold-worked high nitrogen austenitic stainless steel by nitric acid passivation. *J. Electrochem. Soc.* **166**, 365–374 (2019).
70. Sun, S. C. et al. The synthesis and electrochemical behavior of high-nitrogen nickel-free austenitic stainless steel. *J. Mater. Eng. Perform.* **23**, 3957–3962 (2014).
71. Wang, G. H., Jiang, Y. Q. & Guo, C. A. Effect of nitrogen content on the corrosion resistance of high-nitrogen austenitic stainless steel for nonmagnetic drill collar in a harsh service environment. *Int. J. Electrochem. Sci.* **17**, 220656 (2022).
72. Vignal, V., Krawiec, H. & Heintz, O. Passive properties of lean duplex stainless steels after long-term ageing in air studied using EBSD, AES, XPS and local electrochemical impedance spectroscopy. *Corros. Sci.* **67**, 109–117 (2013).
73. Grabke, H. J. The role of nitrogen in the corrosion of iron and steels. *ISIJ Int.* **36**, 777–786 (1996).
74. Yu, C. Y. Analysis of the effect of nitrogen on the spot corrosion resistance of stainless steel. *Corros. Prot. Petrochem. Ind.* **29**, 23–27 (2012).

ACKNOWLEDGEMENTS

This work was financially supported by the National Natural Science Foundation of China (Nos. 52001142, 52005228, 51801218, and 51911530211), Science Foundation

of Jiangsu Province (No. BK 20180984), GDAS' Project of Science and Technology Development (2022GDASZH-2022010103).

AUTHOR CONTRIBUTIONS

F.G. and L.Y.: Investigation, formal analysis, and writing—review and editing. F.G. and J.C.: Conceptualization, writing—review and editing. H.Z. and Z.Z.: Formal analysis and investigation. L.Z.: Sample preparation. Y.Q. and J.C.: Conceptualization, supervision.

COMPETING INTERESTS

The authors declare no competing interests.

ADDITIONAL INFORMATION

Correspondence and requests for materials should be addressed to Yanxin Qiao, Jian Chen or Zhibin Zheng.

Reprints and permission information is available at <http://www.nature.com/reprints>

Publisher's note Springer Nature remains neutral with regard to jurisdictional claims in published maps and institutional affiliations.



Open Access This article is licensed under a Creative Commons Attribution 4.0 International License, which permits use, sharing, adaptation, distribution and reproduction in any medium or format, as long as you give appropriate credit to the original author(s) and the source, provide a link to the Creative Commons license, and indicate if changes were made. The images or other third party material in this article are included in the article's Creative Commons license, unless indicated otherwise in a credit line to the material. If material is not included in the article's Creative Commons license and your intended use is not permitted by statutory regulation or exceeds the permitted use, you will need to obtain permission directly from the copyright holder. To view a copy of this license, visit <http://creativecommons.org/licenses/by/4.0/>.

© The Author(s) 2023